

pubs.acs.org/Macromolecules Article

# Understanding the Aggregation and Flow Response of Donor–Acceptor Conjugated Polymers

Justin J. Kwok, Giridar Vishwanathan, Kyung Sun Park, Bijal B. Patel, Dongqi Zhao, Gabriel Juarez, and Ying Diao\*



Cite This: Macromolecules 2022, 55, 10153-10166



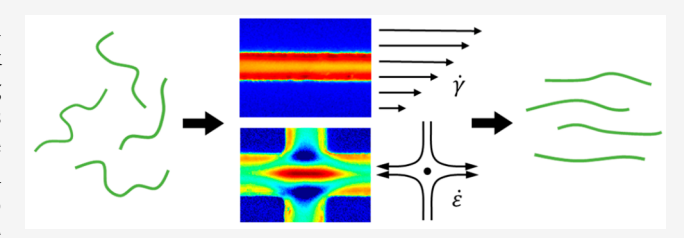
**ACCESS** I

III Metrics & More

Article Recommendations

s Supporting Information

**ABSTRACT:** Fluid flow is an inherent aspect of solution processing of conjugated polymers. Much of the existing work investigating the effect of flow has been phenomenological, lacking a direct and quantitative connection between the flow gradients and measurable quantities of the conformation or alignment of the conjugated polymers in solution. Furthermore, while aggregation of conjugated polymers in solution has been demonstrated to result in highly aligned thin films, there are few studies that probe the interplay between the structures that form during aggregation



and flow-induced alignment during processing. Here, we explore in detail the influence of flow type, solution aggregation, and concentration on the flow-induced alignment of conjugated polymers. We apply a microfluidic platform to systematically subject the conjugated polymer solution to large and controllable shear and extensional strain rates and use flow-induced retardance (birefringence) measurements to characterize the degree of alignment. By using flow-induced retardance in combination with small-angle X-ray scattering (SAXS) and electron microscopy of freeze-dried solutions, we can determine the solution state structure and clearly demonstrate the interplay between solution aggregation and fluid flow. We determine the overall relaxation time of the material and the strengths of shear and extensional flows required to align conjugated polymer aggregates. Furthermore, we find that although enhanced aggregation can facilitate flow-induced alignment, the type of aggregation and the presence of interparticle interactions at higher concentrations can diminish the effectiveness of flow. The results here demonstrate that there is a complex interplay between the conjugated polymer solution state and fluid flow and that simply increasing the conjugated polymer's aggregation, concentration, or the strength of flow does not necessarily lead to better or more effective alignment in solution. A careful understanding of the synergy between these two aspects can help to establish design rules in solution processing for improving conjugated polymer film morphology.

#### INTRODUCTION

Solution processability is a key advantage of conjugated polymers because it enables the production of organic optoelectronic devices in a high-throughput and energyefficient manner. In solution processing, conjugated polymers traverse a complex assembly pathway from the initial ink solution all the way to the solid film. The multiscale assembly throughout this process must be carefully controlled to improve thin film morphology and device performance. It is then important to understand what is the initial state of the conjugated polymer solution and how the solution processing directs further assembly. Many studies have focused on tuning the solution state of conjugated polymers prior to processing. The use of solution aggregation through methods such as applying UV light, 1-3 ultrasonication, 4,5 tuning solvent quality, 6,7 or forming liquid crystalline mesophases 8,9 has been shown to promote the formation of fibrillar or rodlike aggregates. The formation of these initial aggregates enhances alignment and directs further aggregation of the conjugated polymers as they form thin films. These works have hinted toward the synergistic effects of solution aggregation and flow during solution processing to enhance orientational order in printed films. For example, Choi et al.<sup>3</sup> studied the combined effects of solution shearing and aggregation on solutions of P3HT nanowires formed through UV irradiation and solution aging. Separately, the solution shearing and nanowire aggregation led to improved alignment and mobility in the printed films compared to pristine solutions and spin-coated films, while a combination of both led to the highest improvement overall. Additionally, Wang and Reichmanis et al.<sup>2</sup> employed UV irradiation during solution coating with microstructured blades that induce strong local shear and extension. They found the combined effect led to enhanced

Received: July 1, 2022 Revised: October 1, 2022 Published: November 8, 2022





crystallization and alignment of P3HT. These results highlight the fact that the conjugated polymer solution state, fluid flow during processing, and their interplay can be harnessed to improve the effectiveness of solution processing.

Despite the fact that fluid flow is ubiquitous to all solution processing methods, the effect of flow gradients on controlling the alignment and assembly of conjugated polymers is not well understood. Much of the work regarding the flow effect on conjugated polymers has been phenomenological, such as correlating the effect of printing speed 12,13 or the use of a novel printing head 2,14-16 with ex situ characterizations of film morphology. These works have alluded to the importance of flow during solution processing as it can direct the alignment and crystallization of conjugated polymers. 17,18 However, only a few works have performed a more mechanistic study of the effect of flow gradients on alignment. Wie and Mackay et al. 19 have shown that the continuous application of steady shear to concentrated P3HT solutions can promote the growth of long, crystalline fibrils. In our prior work,<sup>20</sup> we used finite element simulation and experiments to show how the flow field and shear rate in the meniscus dictates conjugated polymer assembly and subsequent morphological transitions during printing, such as highly aligned films produced at intermediate printing speeds. These results have highlighted the importance of fluid flow during solution processing, but it remains to be seen how the flow type and strength directly impact the conjugated polymer solution state conformation or alignment in a quantifiable manner.

In this work, we study flow-induced alignment in conjugated polymer solutions by systemically subjecting the solution to controlled amounts of shear and extensional strain rates. To quantify the alignment, we measure the flow-induced retardance (birefringence) of the conjugated polymer solution as it flows through the shear and extensional microchannels. This technique has been used to characterize the deformation of polymers as they are subjected to flow. 21-24 Modern applications of this technique have combined flow birefringence with microfluidics.<sup>25–28</sup> In particular, the works of Haward<sup>29–31</sup> with Odell,<sup>32,33</sup> McKinley,<sup>34–36</sup> and Shen<sup>36–38</sup> have demonstrated that flow birefringence can be used to understand properties including relaxation time, polymer extension, and flow instabilities for a variety of complex fluids such as synovial fluid, wormlike micelles, atactic polystyrene, and cellulose nanocrystal rods. However, this technique has not been applied to conjugated polymer solutions.

Here, we present, for the first time, a systematic study of the effect of flow type and strength on aligning fibril aggregates of a high-performance donor-acceptor conjugated polymer. We use a isoindigo-bithiophene-based polymer (PII-2T) which has demonstrated applications in organic field effect transistors<sup>20,39</sup> and solar cells. 40,41 PII-2T derivatives also have further applications in chemical sensors, thermoelectrics, bioimaging, and so on. 42 Furthermore, the equilibrium solution aggregation state of PII-2T has been studied in our previous work.<sup>43</sup> To achieve flow-induced alignment, we developed microfluidic devices to access very high shear ( $\sim 10^6 \text{ s}^{-1}$ ) and extensional  $(\sim 10^5 \text{ s}^{-1})$  strain rates that have not been accessed before in prior microfluidic flow birefringence studies. Such high strain rates are necessitated by the rapid relaxation of conjugated polymer aggregates in solution. Using microfluidics in combination with in situ retardance measurements, we can directly quantify the dependence of alignment on varying flow conditions. Furthermore, to study the effect of the solution

state on flow-induced alignment, we varied the concentration and also tuned the solution aggregation by adding a poor, polar solvent, resulting in longer and more rigid fibril aggregates as determined by freeze-dried imaging and small-angle X-ray scattering (SAXS). Our study reveals the complex interplay between fluid flow and the conjugated polymer aggregation and its effect on flow-induced alignment, finding that simply increasing flow strength or aggregation does not necessarily lead to improved alignment. The results here can be used to inform design rules for solution processing to leverage potential synergies and improve film morphology in an efficient manner.

#### EXPERIMENTAL SECTION

Materials and Molecular Weight. The isoindigo-bithiophene-based polymer (PII-2T) was synthesized as previously reported. The molecular weight ( $M_{\rm n}=19883,\,M_{\rm w}=61700,\,{\rm PDI}=3.1)$  was characterized using high-temperature gel permeation chromatography at 150 °C in trichlorobenzene. The polymer solutions were prepared by dissolving the polymer in either chlorobenzene (anhydrous, 99.8%; Sigma-Aldrich Inc.) or a mixture of chlorobenzene and 10% v/v dimethylformamide (99.9%; Fisher Scientific). The solutions were then stirred at 80 °C for at least 12 h prior to use. After heating, the solutions were removed to room temperature for 15 min prior to being used in all experiments.

Microfluidic Device Fabrication. We developed microfluidic devices to test small volumes (<100  $\mu$ L) of conjugated polymer solution containing harsh organic solvents at high strain rates and pressure while maintaining device rigidity and optical transparency. For shear experiments, we use narrow microchannels that are 28  $\mu$ m wide and 25  $\mu$ m tall. To minimize pressure drop, this narrow region is only 250  $\mu$ m long and connects to large microchannels 500  $\mu$ m wide on both sides. To minimize extensional flow resulting from the 500 to 28  $\mu$ m contraction, the channel walls follow a hyperbolic shape which maintains a lower maximal extensional strain rate compared to an abrupt or linear contraction. For extensional flow experiments, we use a cross-slot design with microchannels 42  $\mu m$  wide and 25  $\mu m$  tall. Linear contractions were used to allow for wider channels (500  $\mu$ m wide) before and after the cross slot to reduce the device's pressure drop. The device was fabricated using 1 mm thick glass slides (for retardance experiments) or thin glass coverslips (for microparticle tracking velocimetry) for the top and bottom surfaces. Inlet and outlet holes were drilled into the top glass surface, and then both glass surfaces were functionalized with 3-(trimethoxysilyl)propyl methacrylate silane (98%; Sigma-Aldrich Inc.). A perfluoropolyether (PFPE) with urethane methacrylate end groups (Fluorolink MD700) was used to define the microchannel. Two different fabrication processes were used depending on whether the top and bottom surfaces were thick 1 mm glass slides or thin coverslips (Figures S1 and S2). The thick 1 mm glass slides and chemical bonding of the solvent resistant PFPE to methacrylate-functionalized glass were necessary to allow for a microfluidic device that could withstand both the high pressure and organic solvent swelling while maintaining optical transparency and preventing stress-induced birefringence of the glass windows. To make fluidic connections, 30 gauge polytetrafluoroethylene tubing (0.012 in. ID  $\times$  0.030 in.) was flanged and clamped against the drilled inlet/outlet ports using a Viton O-ring (Dash no. 001, Square profile). For more information about the microfluidic device fabrication see Section S1 of the Supporting Information.

High-Speed Microparticle Tracking Velocimetry ( $\mu$ -PTV).  $\mu$ -PTV was used to measure the maximum extension and shear rates inside the cross-slot and narrow microfluidic channels, respectively, for flow rates of 1–20  $\mu$ L/min. Cross-linked polystyrene tracer particles (Spherotech PPX-10-10) of diameter 1  $\mu$ m were mixed with the samples corresponding to a mean interparticle separation of 10  $\mu$ m. Brightfield imaging with a 20× magnification lens (Nikon Plan Fluor) and a depth of field 2.5–4.5  $\mu$ m was used along with a high-

speed camera (Edgertronic SC2+) of a maximum frame rate of 31000 fps and a minimum exposure time of 10  $\mu$ s. The resulting resolution is 0.67  $\mu$ m/pixel, and the maximum particle displacement per frame is 17  $\mu$ m/frame at 20  $\mu$ L/min as compared to a field of view that spans 170  $\times$  68  $\mu$ m<sup>2</sup> at 31000 fps. A custom-built MATLAB code that incorporates topological constraints and symmetries in the flow field was used for accurate tracking at these extreme flow conditions. Higher flow rates could not be used due to the limitations on the field of view and frame rate inherent to the camera.

In Situ Retardance Measurements. The retardance of the PII-2T polymer solution was measured as it flowed through the microfluidic device. The retardance was measured using white light in an optical microscope (Nikon Ci-POL) equipped with two opposite-handed circular polarizers facing each other and oriented orthogonally to each other with the microfluidic device placed in between them, a configuration also known as a circular polariscope. The retardance  $\delta$  is proportional to the birefringence  $\Delta n$  through  $\delta = \frac{2\pi\Delta nd}{r}$  where d is the sample thickness and  $\lambda$  is the wavelength of light. Birefringence occurs due to the anisotropy of a material's refractive index as it becomes aligned. The measured retardance is an average over the spectral composition of the light source. Additionally, considering that our microchannels have widths of similar order to its height, the flow and the subsequent birefringence along a vertical slice of the microchannel are not uniform, and so the retardance is also an average over each vertical position in the microchannel. For these reasons, we do not convert retardance to birefringence. However, because the light source and the microchannel height are kept constant for all experiments, we can still accurately compare the measured retardance values. To accurately measure the retardance, we modeled the optical system and its output polarization state with imperfect linear polarizers and an arbitrarily polarized light source using Mueller matrices. We then developed a procedure where multiple measurements can be combined to cancel out the contributions arising from the imperfections in the optical setup. For more information about the retardance measurement theory and procedure see Section S2 of the Supporting Information. For shear flow experiments, the polymer solutions were flowed at volumetric flow rates of 1-260  $\mu$ L/min, corresponding to shear strain rates of 5950-1550000 s<sup>-1</sup>. For extensional flow experiments, the polymer solutions were flowed at volumetric flow rates of 1-140  $\mu$ L/min, corresponding to extensional strain rates of 655-91700 s<sup>-1</sup>. At flow rates above 140  $\mu$ L/min, the presence of birefringent "pipes" can occur where the centerline birefringence reduces as a result of flow modification from the polymer which lowers the extensional strain rate, making it unreliable to quantify at these conditions. 45,46

Small-Angle X-ray Scattering (SAXS) Experiments. SAXS experiments were performed at the 12-ID-B beamline of the Advanced Photon Source at Argonne National Laboratory using an X-ray beam energy of 13.3 keV. A Pilatus 2M detector was used at sample-to-detector distances of 3.6 m. The polymer solution SAXS experiments were performed using a flow cell to prevent beam damage and enable longer exposure times. The flow cell was constructed using a 1 mm diameter quartz capillary connected to PTFE tubing using PTFE heat shrink tubing. One tubing end was connected to a syringe pump which cycled the polymer solution back and forth through the capillary at 50  $\mu$ L/min (linear velocity of 1 mm/s) within the capillary while a series of 0.1 s exposures with 3 s delays were accumulated for a total exposure time of approximately 1-2 s. Each series of 0.1 s exposures were inspected to ensure that there was no beam damage as characterized by a systematic variation in the scattering profiles with time. Each polymer solution and its neat solvent background were scanned successively at the same position of the same flow cell to ensure that the instrumental "empty cell" scattering was consistent. Such a procedure was necessary due to the weak scattering of our conjugated polymer relative to chlorinated solvent to ensure proper background subtraction. The 2D scattering patterns were isotropic indicating that the flow in the 1 mm capillary did not induce alignment of the conjugated polymer materials. The

2D scattering patterns were then reduced, background subtracted, and averaged using the beamline's MATLAB package.

Freeze-Drying and Scanning Electron Microscopy (SEM) Measurements. We use a freeze-drying method to directly capture the structure of aggregates in solution, which are then imaged using SEM. For the freeze-drying process 2  $\mu$ L of polymer solution was sandwiched between a bare Si substrate and a glass coverslip. The sandwiched sample is first submerged in liquid mixture of 63% propane and 37% ethane and then stored in liquid nitrogen. Because this mixture has a larger heat capacity than liquid nitrogen, it can quickly freeze the sample without boiling off and therefore prevent aggregation during the cooling process.<sup>47</sup> In samples frozen with liquid nitrogen alone, solvent crystallization is observed whereas samples frozen in the liquid propane/ethane mixture exhibit amorphous frozen solvent (as observed under cross-polarized optical microscopy). The top coverslip is separated while submerged in liquid nitrogen, and the sample is then quickly transferred to a sealed Linkam stage chamber (LTS420) which is held at −100 °C in a nitrogen atmosphere. The temperature is raised to -80 °C (0.5 °C/ min) for chlorobenzene and 90% chlorobenzene/10% dimethylformamide solutions while a vacuum is applied for ~6 h to fully sublimate the solvent while preventing melting. The sample is then imaged by SEM (JEOL JSM-7000F) at 25 kV accelerating voltage.

**Viscosity Measurements.** Because of the small amounts of synthesized conjugated polymer material, we measured the viscosity of polymer solutions using only a few microliters. We used the method developed by Srivastava and Burns<sup>48</sup> where a solution is drawn into a microchannel by capillarity and its free surface is tracked to calculate its viscosity. We used a microfluidic glass capillary with a rectangular channel 200 μm wide and 20 μm high (Microslide 5002-050, Wale Apparatus). The capillaries were placed in a small chamber saturated with chlorobenzene vapor. Approximately 5–10 μL of conjugated polymer solution was pipetted onto an open end of the capillary. A camera was used to record the solution as it flowed into the microfluidic capillary. Using the procedure from Srivastava and Burns, <sup>48</sup> we determined the position L and velocity  $\nu$  of the free surface over time and calculated the viscosity  $\eta$  of the solution at low velocities using the equation

$$\eta = \frac{h^2}{S} \frac{1}{\frac{2}{3} + \frac{1}{3n}} \frac{\Delta P}{\nu L} \tag{1}$$

where h is the height of the microchannel, S is a constant that depends on the aspect ratio of the microchannel cross section, n is the power law fluid exponent, and  $\Delta P$  is the capillary pressure. The factor  $h^2/S$  was determined to be  $7.5 \times 10^{-10}$  m/s using the pure chlorobenzene solvent. The capillary pressure is determined from the height h and width w of the microchannel as well as the surface tension of the fluid  $\sigma$  and its contact angle  $\theta$  according to the equation

$$\Delta P = 2\sigma \cos \theta \left(\frac{1}{h} + \frac{1}{w}\right) \tag{2}$$

#### ■ RESULTS AND DISCUSSION

**Determination of Experimental Shear and Extensional Strain Rates.** To investigate the effectiveness of both shear and extensional flow on the alignment of our conjugated polymer, we used microfluidic devices to reach shear rates up to  $\sim 10^6~\rm s^{-1}$  and extensional strain rates up to  $\sim 10^5~\rm s^{-1}$  to observe flow-induced retardance (birefringence) of our conjugated polymer. Such strain rates are significantly higher than those explored in prior work on microfluidic flow birefringence and required microchannels orders of magnitude smaller. Shear was achieved by flow through narrow straight channels, and extension was achieved through the use of a cross-slot geometry with opposing inlets and outlets. For this work, the term shear rate refers to the shear rate at the walls of the straight channel, and the term extensional strain rate refers

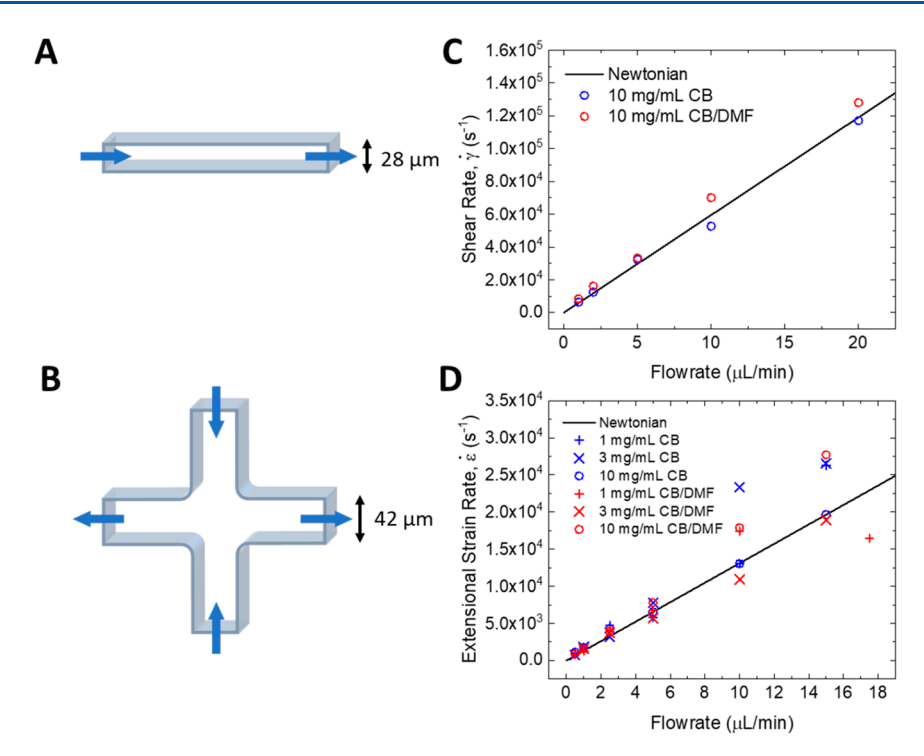


Figure 1. Schematic and  $\mu$ -PTV results for shear and extensional microchannels and retardance imaging setup. Dimensions of straight channel for shear (A) and cross-slot channel for extension (B). Both types of microchannels have heights of 25  $\mu$ m. Experimental shear rates at the channel wall (C) and extensional strain rates at the cross-slot stagnation point (D) for PII-2T CB and CB/DMF solutions determined by  $\mu$ -PTV. The expected theoretical shear and extensional strain rates are shown by the black line, showing good agreement.

to the extensional strain rate at the stagnation point of the cross-slot. Schematics of the shear and extensional microchannels used are shown in Figures 1A and 1B, respectively. To verify the true experimental shear and extensional strain rates produced in the microfluidic device, we used high-speed microparticle tracking velocimetry ( $\mu$ -PTV). An accurate measure of the strain rates is necessary to accurately quantify the relaxation time of the material. Because of the extremely high velocities, we were only able to characterize the shear rates at flow rates up to  $20~\mu$ L/min instead of the full range up to  $260~\mu$ L/min used in the retardance experiments. We emphasize that even with the use of a high-speed camera, we were limited by the frame rate (31000 fps) due to the extremely high velocities and strain rates. For a Newtonian fluid the theoretical wall shear rate  $\dot{\gamma}$  for a rectilinear channel is  $\dot{z}^{49}$ 

$$\dot{\gamma} = \frac{2}{3}\pi^2 Q \frac{h^2 + w^2}{(hw)^2 (h + w)} \tag{3}$$

where Q is the volumetric flow rate, w is the channel width, and h is the channel height. The  $\mu$ -PTV shear experiments were performed using the highest concentration in this work (10 mg/mL) to check for rheology-induced instabilities or modifications to the flow profile. The experimental and theoretical shear rates are shown in Figure 1C for PII-2T solutions in both chlorobenzene (CB) and 90% chlorobenzene/10% dimethylformamide (CB/DMF), which exhibit different aggregation states. From our prior work, <sup>43</sup> the solution state of PII-2T in pure CB consists of elongated, semiflexible fibril aggregates in addition to a separate population of dispersed polymer chains. As will be discussed later, the solution state in CB/DMF is similar but consists of fibril aggregates that are more rigid, have improved lamellar

order, and also form large agglomerates. For both 10 mg/mL solutions, the experimental shear rate agrees well with the theoretical Newtonian shear rate for the accessible flow rates. We therefore use this relation to determine the shear rates for the retardance experiments over the full flow rate range. Likewise, we used  $\mu$ -PTV to determine the experimental extensional strain rates in the cross-slot microchannels for flow rates up to 35  $\mu$ L/min (full range up to 140  $\mu$ L/min). For a Newtonian fluid, the extensional strain rate at the cross-slot's stagnation point  $\dot{\varepsilon}$  has been shown to follow<sup>30</sup>

$$\dot{\varepsilon} = \frac{1.7Q}{hw^2} \tag{4}$$

where Q refers to the total volumetric flow rate of both opposed inlets. The extensional strain rate was measured over the concentration range used in this work at 1, 3, and 10 mg/mL for both PII-2T in CB and CB/DMF solutions. The experimental and theoretical extensional strain rates are shown in Figure 1D. Although there is some variation due to frame rate limitations at the higher flow rates, the deviations are not systematic in terms of either the concentration or the flow rate, and they do not vary exponentially as would be expected for instabilities or strong modifications to the flow structure. While the frame rate limitations of our high-speed camera make it difficult to accurately measure the higher strain rates, the experimental and theoretical Newtonian strain rates agree well at low flow rates so we use eq 4 to determine the extensional strain rates for the retardance experiments.

Flow-Induced Retardance of PII-2T Aggregates in Shear and Extensional Flow. Having characterized the strain rates generated by our microfluidic devices, we next use retardance imaging to quantify the degree of alignment in our PII-2T solutions as a function of shear and extensional strain

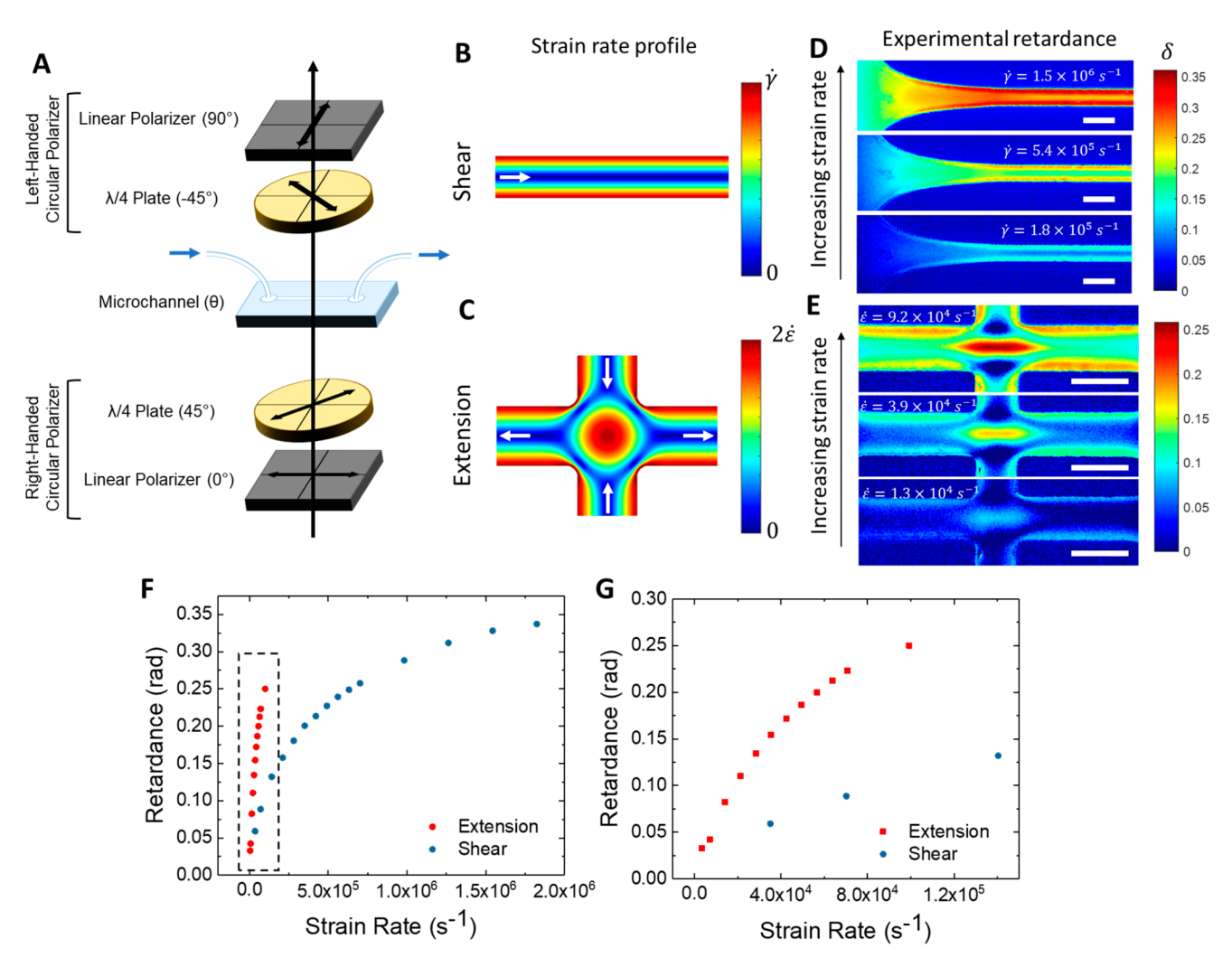


Figure 2. Comparison of PII-2T/CB 10 mg/mL flow-induced retardance under shear and extensional flow. (A) Retardance imaging setup consisting of opposing, orthogonally aligned right- and left-handed circular polarizers placed before and after the microfluidic channel, respectively. The calculated strain rate profile throughout the channel is shown for the straight channel (B) and the cross-slot channel (C). Examples of the 2D retardance throughout the channels at varying strain rates for shear (D) and extension (E). Scale bar is 50  $\mu$ m. The retardance near the walls and at the stagnation point are plotted against the strain rate in (F) with a zoom-in of the extensional data (dashed box) in (G).

rate for different aggregation types and concentrations. A schematic of the retardance imaging experimental setup is shown in Figure 2A. More information about the retardance imaging setup and procedure can be found in the Experimental Section and in Supporting Information Section S2.

Using retardance imaging, we first compare the polymer solution state response to shear and extensional flow. Solutions of PII-2T in CB at 10 mg/mL were flowed through the microchannels to measure flow-induced retardance resulting from the shear and extensional strain rate. Figure 2B,C depicts the expected strain rate in the microchannels, which corresponds to the magnitude of the rate-of-strain tensor,  $|E| = \sqrt{2E \cdot E}$ , as calculated using COMSOL. The maximum shear and extensional strain rate occur at the walls and at the stagnation point, respectively, where the retardance is measured. Experimental retardance imaging throughout the channel is shown for several different strain rates for the narrow (shear) and cross-slot (extensional) microchannels in Figure 2D,E. The retardance intensity correlates well with regions of high strain rate for both cases. Specifically, for the cross-slot flow, the retardance correlates to regions of extension where the fluid exits the stagnation point as opposed to regions of compression where the fluid enters the stagnation point. The retardance for both shear and extensional flow is plotted against the strain rate in Figure 2F with a zoomed-in plot of the extensional data (dashed box) shown in Figure 2G. It can clearly be seen that extensional flow is significantly more effective at aligning and/or stretching the conjugated polymer fibrils compared to shear, requiring 3-6 times less strain rate to achieve the same retardance. The rate of increase of alignment per unit increase in strain rate is also much larger. Considering shear contains both extensional deformation and rotation motion, it is likely that the rotational component of shear diminishes its effectiveness to achieve high alignment compared to pure extension, which completely lacks rotation. Such behavior qualitatively matches previous work demonstrating extension to be more effective at aligning rods compared to shear.<sup>50</sup> A more recent example of this has been demonstrated by Calabrese, Haward, and Shen<sup>38</sup> where they used flow-induced birefringence to characterize the alignment of cellulose nanocrystal rods undergoing Brownian rotational diffusion, finding an extensional strain rate to induce

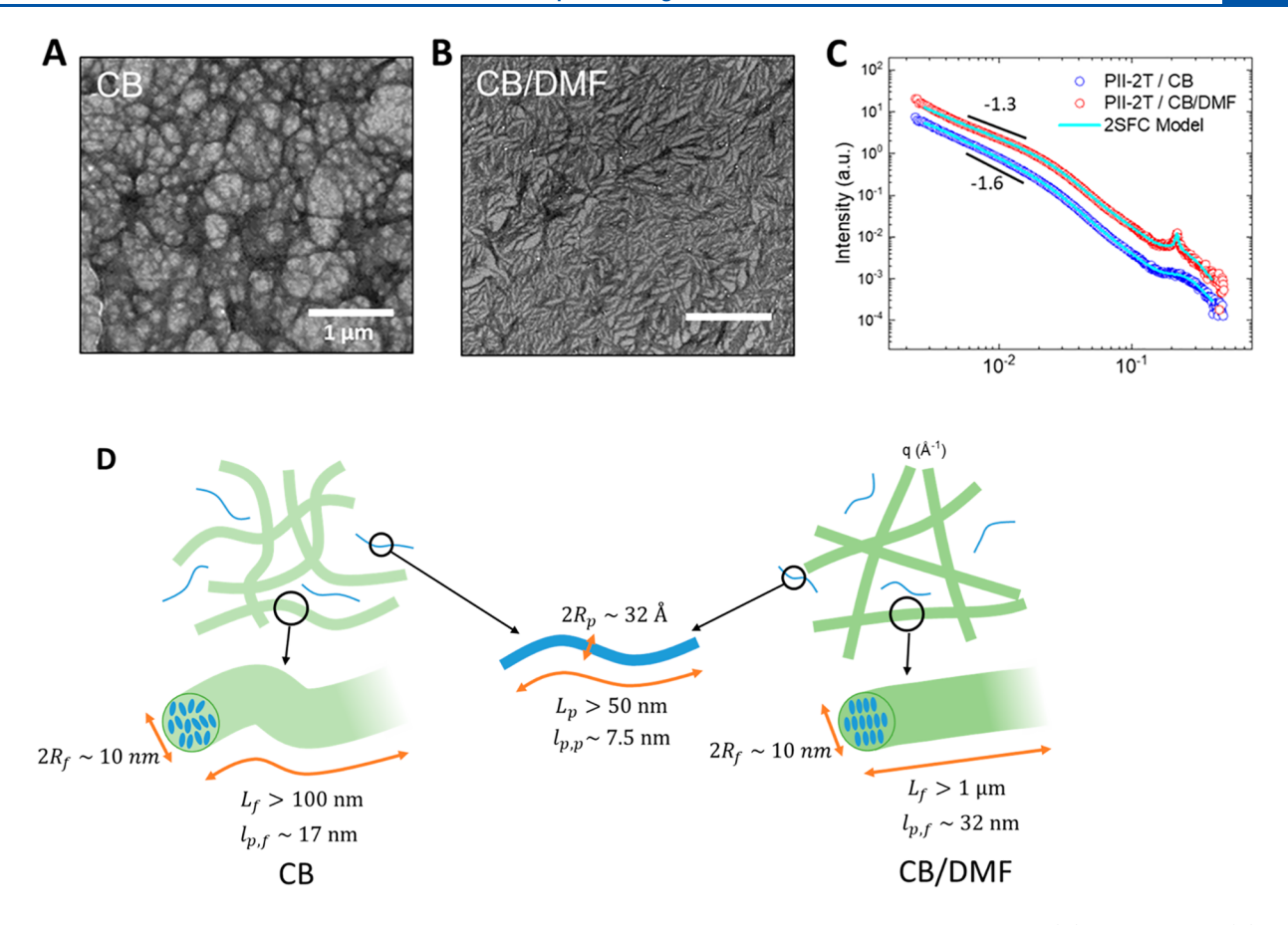


Figure 3. Solution aggregation of PII-2T in CB and CB/DMF. SEM imaging of freeze-dried PII-2T samples from CB (A) and CB/DMF (B). Scale bars are 1  $\mu$ m. (C) Comparison of SAXS profiles and fitting of PII-2T in CB and CB/DMF (shifted for clarity). (D) Scheme of the solution state aggregation in both CB and CB/DMF. The aggregation of PII-2T in CB/DMF consists of fibrils that are more rigid and have higher lamellar order than those in pure CB.

a 4 times higher degree of alignment compared to shear around the onset of flow-induced birefringence.

Solution State Aggregation of PII-2T in CB and CB/ DMF. Next, we compare how different types of solution aggregation can affect the alignment response to shear and extensional flow. While the effects of poor solvents and solution aggregation on conjugated polymer film morphology have been previously studied and were found to enhance alignment in printed films, 4,51,52 few works have directly probed how conjugated polymers or their aggregates are influenced by flow gradients in solution. To examine this, we add 10% v/v DMF to PII-2T/CB 10 mg/mL solutions to alter and enhance the aggregation of the conjugated polymer, which was also confirmed by the presence of large aggregates seen by optical microscopy (Figure S3). To understand in greater detail how the addition of DMF changes the aggregation state, we performed freeze-dried SEM imaging as well as SAXS. The freeze-drying method was validated in our previous work<sup>43</sup> where the dimensions of freeze-dried aggregates imaged by SEM and AFM were found to agree with dimensions of aggregates in solution determined by SAXS. Freeze-dried SEM images of the PII-2T solution state structure in CB and CB/ DMF are shown in Figures 3A and 3B, respectively. Imaging of PII-2T in pure CB reveals elongated, semiflexible fibril aggregates with diameters on the order of 10 nm and lengths ranging broadly from ~100 nm to several micrometers. Fibril aggregates are also present with the addition of 10% DMF and have similar diameters. However, these fibrils have more

rodlike conformations, indicating higher rigidity. Furthermore, some larger scale agglomerates of rodlike fibrils can also be seen with lengths >1  $\mu$ m (Figure S4).

The SAXS profiles of PII-2T in CB and CB/DMF are shown in Figure 3C. As discussed in our previous work, 43 the scattering profiles can be described by a combination of scattering from fibril aggregates, dispersed polymer chains, and a lamellar structure factor peak. The profiles in CB and CB/ DMF are nearly identical with similar features, such as the Guinier knee at  $q = 0.02 \text{ Å}^{-1}$  corresponding to the fibril radius. Additionally, both scattering profiles indicate the presence of aggregates by the power law region extending into low q as well as the lamellar structure factor peak at high q ( $q \sim 0.22 \text{ Å}^{-1}$ ). However, there are two key differences that the aggregation state in CB/DMF exhibits compared to that in pure CB. The first is the presence of a sharper structure factor peak at 0.22  $Å^{-1}$  which indicates a higher degree of lamellar order within the aggregates formed in CB/DMF compared to CB. The next key difference is the change in slope at low q in the region preceding the fibril cross-sectional Guinier knee at  $q < 0.02 \text{ Å}^{-1}$ which is affected by the persistence length of the fibril aggregate. For PII-2T in CB, the fibril aggregate has a slope of -1.6 while for PII-2T in CB/DMF the slope is -1.3, indicating a higher degree of rigidity. To quantitatively extract the features of the fibril aggregates, we fit using the two semiflexible cylinder (2SFC) model as described in our previous work, 43 with the addition of a second pseudo-Voigt peak for PII-2T in CB/DMF. As the scattering is largely

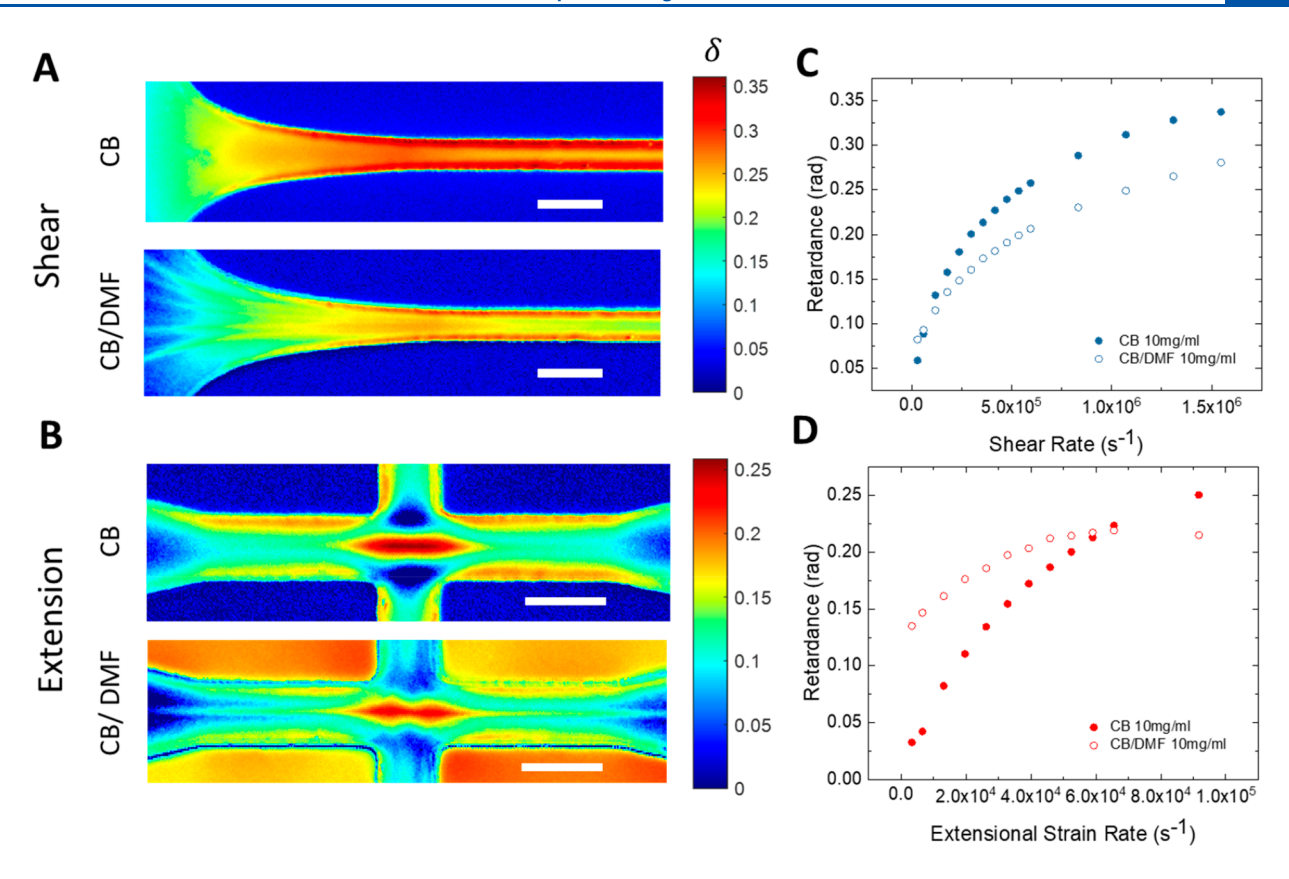


Figure 4. Comparison of flow-induced retardance of PII-2T aggregation in CB and CB/DMF at 10 mg/mL. Examples of 2D retardance throughout the shear (A) and extension (B) channels. The retardance near the walls and at the stagnation point plotted against shear (C) and extensional strain rate (D). Birefringence can exist in the walls due to stress from extended exposure and swelling of DMF. This birefringence does not exist within the channels. Scale bar is 50  $\mu$ m.

insensitive to the polymer contour length  $L_p$  and persistence length  $l_{v,v}$  due to the overshadowing fibril contribution, we fix them to the values of 100 and 7.5 nm from our previous work. We also again find that the pseudo-Voigt peak Lorentzian fraction tended to 1 in both cases during fitting, signifying paracrystalline disorder within the aggregates. The fitting results for PII-2T in CB match our previous results, indicating the presence of fibrillar aggregates with mean diameters of  $2R_f$ = 10 nm and persistence length  $l_{p,f}$  = 17 nm as well as an additional population of dispersed polymer chains which have diameters of  $2R_p = 32$  Å, slightly larger than the lamellar stacking distance. The lamellar peak, fitted with the pseudo-Voigt contribution, is centered at  $q_c = 0.21 \text{ Å}^{-1}$  (d-spacing of 30 Å) and exhibits a FWHM of w = 0.21 Å<sup>-1</sup>, leading to a disorder-associated coherence length of  $l_{coh}$  = 3.0 nm. While this length is the same as the d spacing, this disorder-associated coherence length ultimately stems from the convolution of both size and disorder effects. 53,54 For PII-2T in CB/DMF, the fibril aggregates also have mean diameters of  $2R_f = 10$  nm but are more rigid with a persistence length  $l_{pf} = 32$  nm, in agreement with the shallower slope at  $q < 0.02 \text{ Å}^{-1}$ . The polymer chains have diameters of  $2R_p = 32 \text{ Å}$ , matching the CB solution as expected since the cross section of individual polymers chains in solution should not change much with solvent quality. Additionally, we found it necessary to use two pseudo-Voigt peaks to capture the high-q region as it contains both a sharp peak and broad tails which cannot be captured by a single peak. This indicates that while there is highly ordered lamellar stacking, weak ordering still exists. The broad peak is

centered at  $q_{c1} = 0.20 \text{ Å}^{-1}$  with a FWHM of  $w_1 = 0.18 \text{ Å}^{-1}$  ( $l_{coh} = 3.5 \text{ nm}$ ). The sharp peak is centered at  $q_{c2} = 0.22 \text{ Å}^{-1}$  with a FWHM of  $w_1 = 0.013 \text{ Å}^{-1}$ , leading to a much larger lamellar coherence length of  $l_{coh} = 50 \text{ nm}$ . The more rigid fibril aggregation in CB/DMF compared to that in CB is corroborated by the more rodlike structures seen by freezedried SEM imaging. Using the SAXS and imaging results, we then illustrate a scheme of the PII-2T solution state in both CB and CB/DMF in Figure 3D.

Interplay between Solution State Aggregation and Flow-Induced Alignment. To understand the implications of how this change in solution aggregation can influence flowinduced alignment, we performed similar retardance imaging of PII-2T in CB/DMF at 10 mg/mL for shear and extensional flow. Figures 4A and 4B show the shear and extensional retardance images of the CB/DMF solutions (bottom) in comparison to the pure CB case (top) at the highest corresponding strain rates. The spatial profiles are surprisingly different, with the CB/DMF aggregates being more easily aligned due to having slower orientational relaxation. This is clearly shown in Figure 4B where the retardance streak persists throughout the outlet channels for the CB/DMF solution while it decays quickly outside the stagnation point in the pure CB solution. On the other hand, the CB/DMF solution reaches a lower degree of alignment compared to the CB solution at higher strain rates. This can also be seen in Figure 4A,B where the retardance at the walls for shear and at the stagnation point for extension is lower for CB/DMF compared to CB. Figure 4C,D further demonstrates this as the retardance

versus strain rate is compared between the two solutions for shear and extensional flow. In both shear and extension cases the retardance of the CB/DMF solution is higher at lower strain rates. However, as the strain rate increases, the retardance of the pure CB solution becomes higher.

The drastic difference in the flow response can be attributed to the differing PII-2T fibril aggregation achieved by the two different solvents with the CB/DMF fibrils being both longer and more rigid than those in CB as corroborated by the freezedried imaging and SAXS. These long, rigid, and anisotropic aggregates and agglomerates have significantly longer orientational relaxation times, especially since this time scales with the length nearly to the power of 3, making them easier to align at low strain rates. 55,56 In contrast, the fibril aggregates found in CB are shorter and more flexible, thus having shorter relaxation times and also requiring a degree of stretching prior to alignment.  $^{57}$  Despite this, at higher strain rates the fibril aggregation in CB can achieve a higher degree of flow-induced retardance compared to that in CB/DMF. Considering that the aggregates in CB/DMF are significantly easier to align, the higher alignment of fibril aggregates formed in pure CB at higher strain rates may be due to the internal structure of the aggregates. In other words, despite the CB/DMF aggregates being easier to align at weaker flows, at stronger flows the overall orientational order is ultimately limited by the alignment within the aggregate's internal structure. This then suggests that the internal structure of fibril aggregates in CB is more susceptible to reconformation by flow compared to that in CB/DMF. This process of aligning and/or ordering the aggregate's internal polymer structure can be described by another characteristic relaxation time scale, which should be much shorter than the orientational relaxation time of the overall aggregate and thus corresponding to higher strain rates. Considering that the fibril aggregates in CB are more flexible and are initially more disordered than fibril aggregates in CB/ DMF, it is reasonable to assume that the relaxation time of the internal polymers within the fibrils in CB is slower than that in CB/DMF. Thus, the internal structure of the CB fibrils would be easier to modify and align, resulting in a higher retardance at higher strain rates. These results highlight the importance of not only how the exact nature of solution aggregation influences the structure and ordering of aggregates but also how the size, shape, rigidity, and internal structure of the aggregates can drastically alter its response to flow.

Effect of Concentration on Flow-Induced Alignment. Next, we investigate the effect of concentration on the flow response of PII-2T/CB and PII-2T/CB/DMF aggregates. First, we characterized the viscosity of small volumes of PII-2T/CB solution available using a method where a droplet is drawn into a microfluidic capillary and the position and velocity of the free surface is tracked as it flows in. 48 The specific viscosity versus concentration is shown for PII-2T in CB in Figure 5. (The corresponding viscosity of CB/DMF solutions could not be measured reliably due to agglomerates approaching a size comparable to the capillary.) At around 10 mg/mL, the concentration scaling exponent changes from of 1 to 1.7. The intrinsic viscosity of the solution can also be determined from the slope of  $\eta_{sp}$  vs c in the linear regime using the relation<sup>37</sup>  $\eta_{sp} = [\eta]c$ , which yields a value of  $[\eta] = 0.11$  mL/ mg. This gives another estimation of the overlap concentration  $c^* \sim 1/[\eta]$ , which yields a value of 9 mg/mL and is in agreement with the transition between the scaling regimes. Conventionally, given a solution of dispersed polymer chains, a

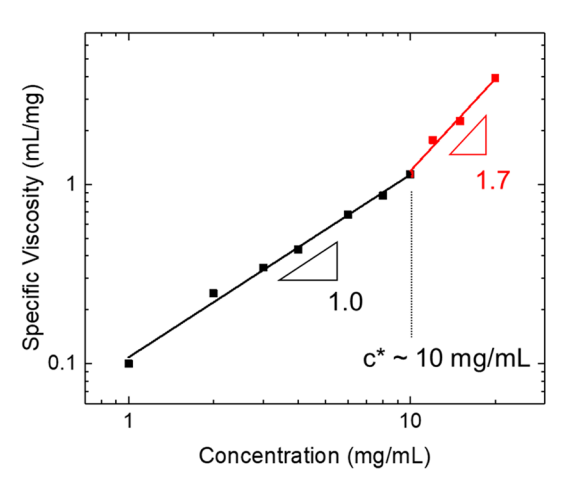


**Figure 5.** Specific viscosity of PII-2T in CB. At low concentrations the scaling exponent of the concentration is 1.0. Around 10 mg/mL the scaling exponent increases to 1.7, indicating the emergence of interfibril interactions.

scaling exponent of 1 is indicative of the dilute regime where the polymer chains do not interact. At around 10 mg/mL, the scaling exponent changes to 1.7, indicating the emergence of polymer interactions at the overlap concentration of  $c^* \sim 10$  mg/mL. While the PII-2T/CB solution contains both fibril aggregates and dispersed polymer chains, the change in scaling at  $\sim\!10$  mg/mL is likely due to fibril interactions as opposed to polymer interactions due to the concentration dependence of retardance occurring at time scales too slow for individual polymer relaxation as discussed later.

The retardance profiles for shear and extension were measured for concentrations ranging from 2 to 10 mg/mL in both CB and CB/DMF solutions. The retardance profiles for each concentration are shown in Figure S5. To compare the relative degree of alignment across different concentrations, we normalize the retardance by concentration to get the specific retardance  $\delta/c$ . This value is proportional to the specific birefringence  $^{58}$   $\Delta n/c$  as well as the birefringence normalized by the birefringence at full extension  $\Delta n / \Delta n_0$  since  $\Delta n_0 \propto c$ , which has been used to characterize a polymer's degree of extension. 36,59 For shear flow, the specific retardance of PII-2T in CB and CB/DMF is shown in Figures 6A and 6B, respectively. For CB, the normalized retardance profiles overlap from 2 to 4 mg/mL and then begins to decrease with increasing concentration. For CB/DMF, the specific retardance decreases throughout, from 2 to 10 mg/mL. The specific retardance for extensional flow of PII-2T in CB and CB/DMF is shown in Figures 6C and 6D, respectively, where the curves largely overlap for all concentrations in both systems. Prior work on the flow birefringence of polymer solutions in extensional flow has shown that the birefringence increases linearly with concentration for dilute solutions (c < $c^*$ ) but sublinearly for semidilute  $(c > c^*)$  range, indicating an inhibition of flow-induced alignment resulting from polymer interaction effects.<sup>58</sup> More recently, this has also been observed directly though the tracking of single DNA relaxation dynamics in extensional flow, where it was found that the fractional extension of the polymer was reduced in the semidilute concentration regime compared to the ultradilute regime.<sup>60</sup> For the case of PII-2T in CB, the shear retardance measurements and the viscometry data support this inference. The specific retardance overlaps at lower concentrations (2, 3,

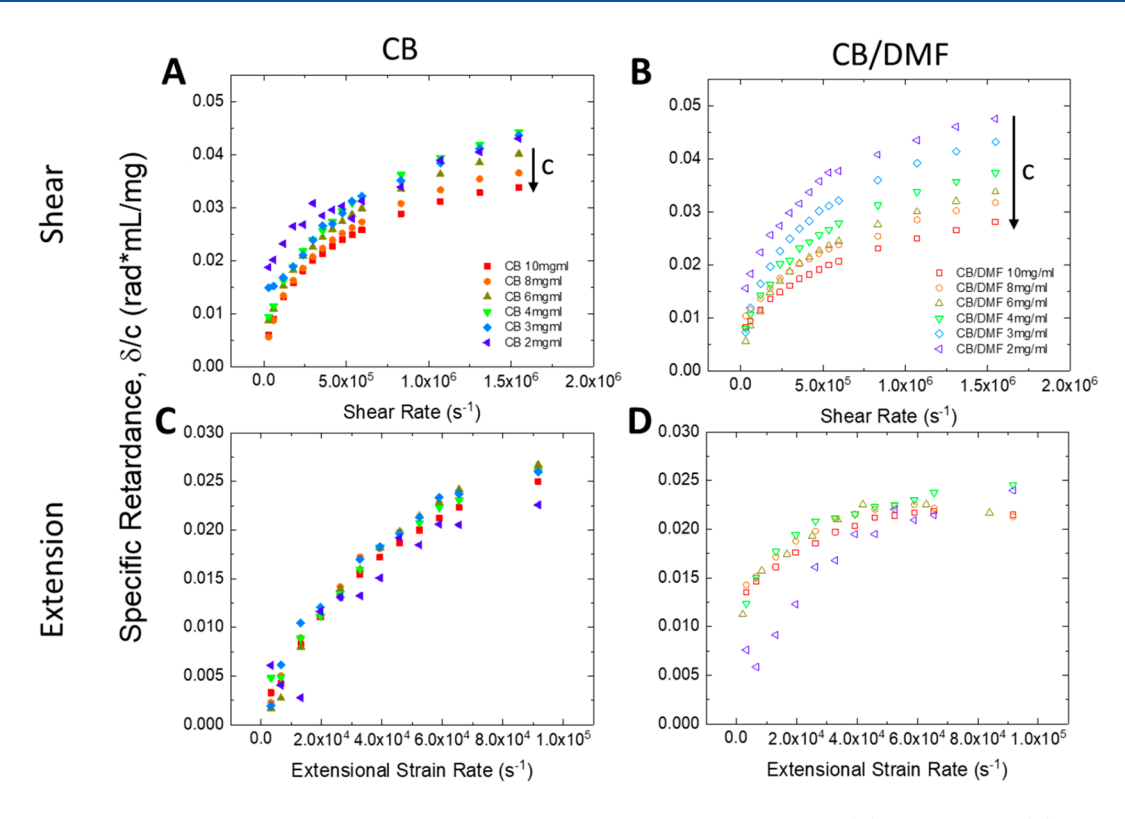


**Figure 6.** Specific retardance curves vs strain rate. The normalized curves for shear flow of PII-2T in CB (A) and CB/DMF (B) show a reduction in the degree of alignment with increasing concentration (indicated by arrow). The normalized curves for extensional flow for PII-2T in CB (C) and CB/DMF (D) do not show significant deviation with the curves collapsing together.

and 4 mg/mL) but begins to decrease at 6 mg/mL and above, indicating that interactions manifest at 6 mg/mL. This agrees with the overlap concentration estimate of ~10 mg/mL obtained from the viscosity measurements. The slight deviation of the onset of interactions can be reasonably attributed to the much stronger shear rates encountered inside the microfluidic device, as compared to the capillary used for viscometry, resulting in polymer and fibril conformations that are more extended. Because the concentration dependence of the specific retardance occurs at strain rates corresponding to time scales too long for polymer relaxation (discussed later), the concentration dependence is likely due to interactions between the large fibril aggregates instead. For the case of PII-2T in CB/DMF, the reason for the monotonic decrease in specific retardance across all concentrations is less clear due to the lack of viscometry data. However, considering that the fibrils in CB/DMF are longer and more rigid than those in CB, such interfibril interactions are likely present as well and would emerge at lower concentrations. Overall, these results indicate that although increasing the concentration produces a higher magnitude of retardance, the actual degree of alignment is inhibited in shear flow as the concentration increases to the point where fibril aggregate interactions emerge.

For extension, the overlap of all curves for both CB and CB/DMF cases suggests that fibril interaction effects are minimal and that there is no inhibition to flow-induced alignment at the extensional strain rates considered here. This may be due to extensional flow lacking the rotational fluid motion that is present in shear flow. However, considering that the extensional strain rates are about 1 order of magnitude lower than the shear rates, it is also possible that the concentration effects are simply not yet prominent. Nonetheless, extensional

flow can achieve higher retardance at lower strain rates where inhibition from interfibril interactions does not occur, making it more effective than shear at inducing alignment.

Characterization of PII-2T Aggregate Relaxation Time. Finally, we characterize the relaxation time of the conjugated polymer solution using the extensional retardance measurements. Estimating the relaxation time of our materials is useful as it provides a quantitative measure of the required strain rate necessary to overcome the relaxation of the material. This is described by the Weissenberg number, which is a dimensionless value that compares the extensional strain rate of a material versus its relaxation time,  $Wi = \dot{\varepsilon}\tau$ . If relaxation is purely orientational, such as for rods, this dimensionless quantity is also sometimes termed the Péclet number. When the strain rate overcomes the relaxation of the material ( $\dot{\varepsilon} > 1/$  $\tau$ ), orientational ordering can occur through extension and/or alignment. Therefore, a value above the critical value of  $Wi \sim 1$ is necessary to achieve orientational ordering. More precisely, studies on flow-induced alignment and extension of macromolecules have found the critical Wi to range from 0.5 to 1.25,31,61,62 To characterize the critical Wi, we subject the solution to extensional flow and measure the spatial decay of the retardance intensity after the polymer solution leaves the stagnation point and flows out through the straight outlet channels along the centerline. It is along this centerline in the outlet channel where both extension and in-plane shear are negligible and do not affect polymer and fibril conformation or orientation. Out-of-plane shearing simply produces a constant retardance baseline along this centerline. Therefore, any change in retardance along this centerline is due to orientational relaxation of the fibril aggregates. Using the centerline velocity, we convert the spatial retardance decay into

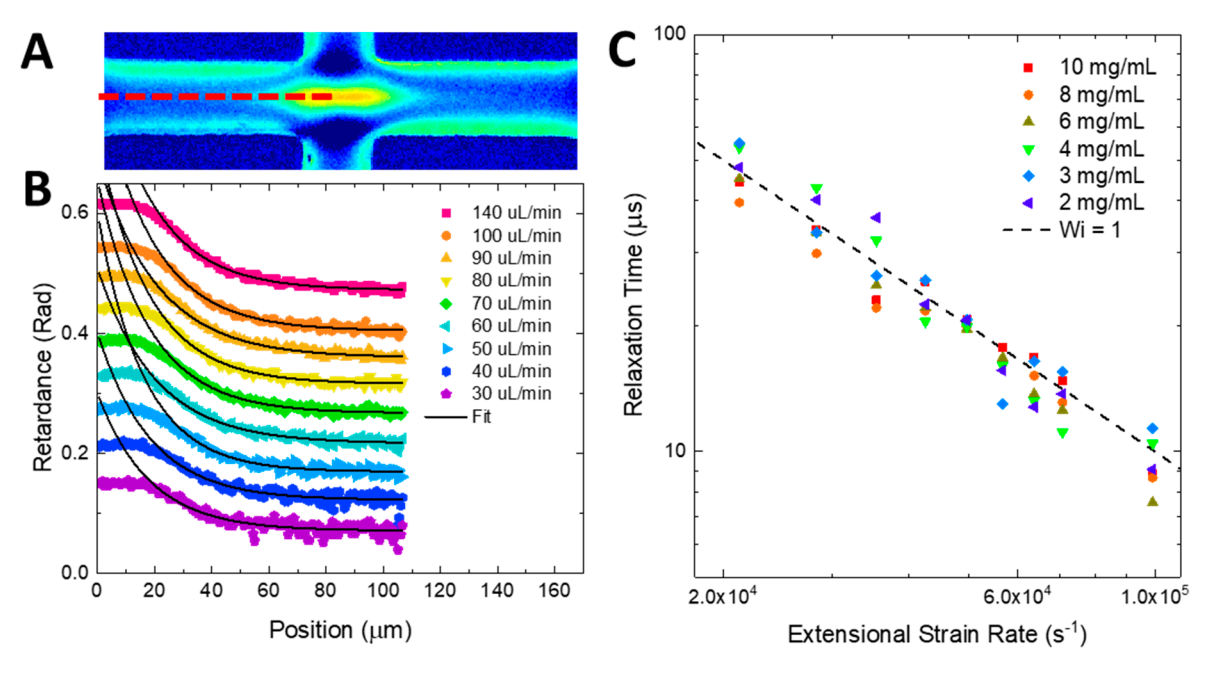


Figure 7. Flow-induced retardance decay. (A) Example of 2D retardance image of PII-2T/CB at 10 mg/mL flowing through the cross-slot microchannel. A red dashed line indicates the centerline where intensity decay is extracted. (B) Example of spatial decay profiles extracted from PII-2T/CB at 10 mg/mL for varying flow rates fitted to an exponential decay (black line). The spatial decays are converted to temporal decays using the centerline velocity. (C) The relaxation time from the temporal decay constant is plotted against the extensional strain rate which closely follows  $Wi \sim 1$ .

a temporal decay. Previous work by Haward and McKinley et al.<sup>34</sup> used the spatial birefringence decay along the outlet centerline (which also follows an exponential decay) to measure the relaxation time of CPyCl/NaSal wormlike micelles, finding it to be in agreement with CaBER (capillary breakup extensional rheometer) experiments. A similar approach has also been used in the direct visualization of individual fluorescently stained  $\lambda$ -DNA where extensional flow is first applied to stretch the macromolecule and then it is stopped while the conformational relaxation is visually tracked over time, also yielding an exponential decay. 62 An example of the retardance imaging is shown in Figure 7A at  $\dot{\varepsilon} = 3.9 \times 10^4$ s<sup>-1</sup> for 10 mg/mL PII-2T/CB with a dashed line indicating the position of the centerline intensity decay. Examples of the decay profiles are shown in Figure 7B with exponential fits starting  $\sim 10 \ \mu m$  after the solution has already entered the outlet channel. The relaxation times from the decay constants are then plotted against the extensional strain rate for all concentrations in Figure 7C. Interestingly, we find that for all conditions the relaxation time is not constant but closely follows the inverse relation  $\tau = 1/\dot{\varepsilon}$ , which indicates a value of  $Wi \sim 1$  is followed in all cases (as shown by the dashed line corresponding to exactly  $\tau = 1/\dot{\varepsilon}$ , or Wi = 1). As the relaxation time decreases with increasing strain rate, this indicates that the material becomes more difficult to align at higher extensional strain rates. This general trend can potentially be explained by a couple of effects. The first is the presence of polydispersity in the fibril aggregates' size. As the extensional strain rate increases, more and more of the shorter fibrils become aligned. Because shorter fibrils have shorter relaxation times, the ensemble average relaxation time measured by the retardance decreases. The second is related to the orientation dependence of rotational diffusion related to the tube model described by Doi, 63 although the interactions here may be due to hydrodynamic interactions as opposed to entanglements

considering the concentrations are just below or at the overlap concentration. As the fibril aggregates align, they become less interacting with each other as the volume around a fibril for which neighboring fibrils do not intersect increases. As a result, the fibrils are more freely able to rotate and so the rotational diffusion coefficient becomes a function of the fibrils' orientation distribution function. Therefore, as fibrils become more aligned at higher strain rates, the rotational diffusion coefficient increases and the orientational relaxation time decreases. This behavior has been observed experimentally by Håkansson et al.<sup>64</sup> where cellulose nanofibrils exhibited a higher resistance to alignment at stronger extensional flows.

To get an estimate of our material's overall relaxation time, we differentiate our retardance versus strain rate curves to yield a relaxation time distribution. As demonstrated by Haward et al., 30,33,35 the birefringence versus strain rate curves are akin to a cumulative distribution with the birefringence at a particular strain rate representing a cumulative amount of polymers being aligned at that strain rate. In these works, the relaxation time is taken to be the inverse of the strain rate, and then the relaxation time is transformed to molecular weight using the power law relation  $\tau \propto M^{\alpha}$ , where the exponent  $\alpha$  is 1.5 for a flexible polymer. However, it has been shown that monodisperse polymer solutions do not exhibit a sudden sharp increase in birefringence with increasing strain rate that would be expected according to this interpretation.<sup>36</sup> Furthermore, direct imaging of DNA in extensional flow has also shown that monodisperse macromolecules undergo varying relaxation trajectories with a distribution of relaxation times. 61,62 With this in mind, we differentiate the retardance curves to yield relaxation time distributions but do not transform them to molecular weight. From the spatial decay results in Figure 7, we have confirmed experimentally that at any particular condition the PII-2T/CB solution exhibits an overall relaxation time that follows the inverse of the extensional strain rate,  $\tau \sim$ 

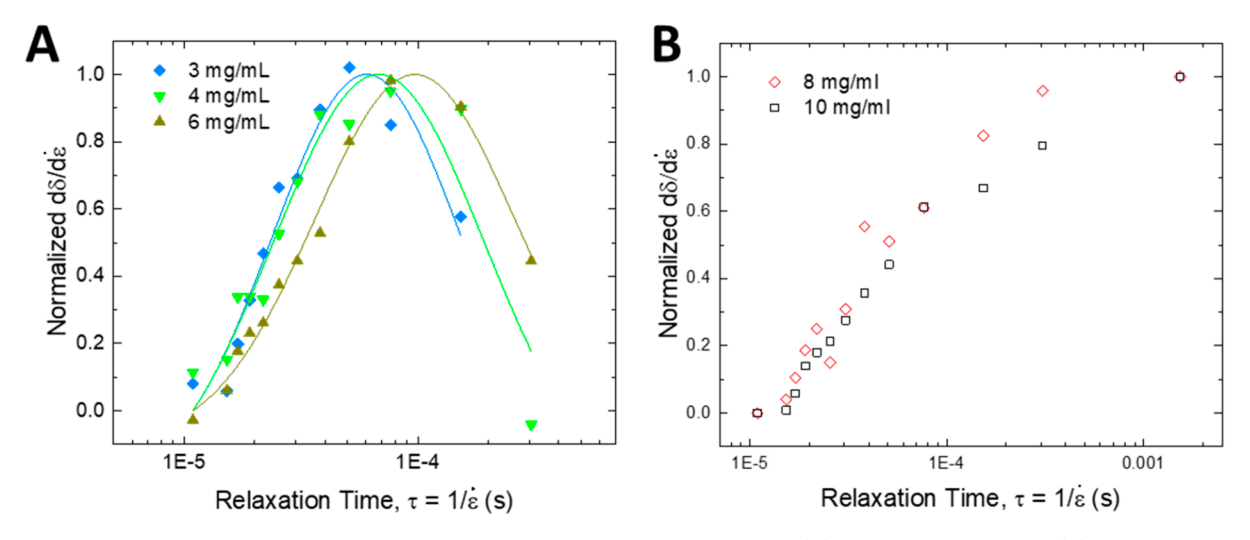


Figure 8. Relaxation time distributions of the PII-2T/CB solution at 3, 4, and 6 mg/mL (A) and 8 and 10 mg/mL (B). Lines are log-normal distribution fits.

 $1/\dot{\varepsilon}$ . Thus, we take the relaxation time to be the inverse of the extensional strain rate after differentiating the retardance profile to get the relaxation time distribution.

The results are shown in Figure 8A, where the peak relaxation time is determined for PII-2T in CB to be 60  $\mu$ s at 3 mg/mL, 68 µs at 4 mg/mL, and 97 µs at 6 mg/mL. As shown in Figure 8B for 8 and 10 mg/mL, the lack of an inflection point in the retardance profile results in the peak relaxation time being undeterminable. However, it must be longer than those at lower concentrations and should therefore be >100  $\mu$ s. This is again in agreement with our observations that the presence of interfibril interactions start to occur as concentration approaches ~10 mg/mL. We do not determine the relaxation time distribution for PII-2T in CB/DMF as we observed alignment and faint birefringence at very weak flows ( $\sim$ 0.02  $\mu$ L/min), indicating a very long relaxation time which is to be expected considering the large size of the fibril agglomeration. Because birefringence was observed below our lowest flow rate, the relaxation time of the CB/DMF aggregates must be greater than the corresponding inverse strain rate, or >1 ms.

We compare the experimental relaxation times against theoretical relaxation times for a single PII-2T polymer. To estimate the relaxation time, we use the relation for Zimm relaxation time<sup>37,65</sup> as well as the rotational diffusion coefficient for wormlike chains. <sup>56</sup> The Zimm relaxation time is given by

$$\tau_Z = \frac{1}{U} \frac{[\eta] M_{\rm w} \eta_{\rm s}}{RT} \tag{5}$$

where  $[\eta]$  is the intrinsic viscosity,  $M_{\rm w}$  is the molecular weight,  $\eta_{\rm s}$  is the solvent viscosity, R is the gas constant, T is the temperature, and U is the universal ratio of the characteristic relaxation time to the longest relaxation time. U depends on the relaxation spectrum of the constitutive model and has values of 2.39 for theta solvents and 1.8 for good solvents, and so for the purpose of estimation we use a value of 2. For the rotational diffusion method, we estimate the rotational diffusion of our polymer using the expression for rods by Broersma, and then we calculate the deviation from this value using the results of Hagerman and Zimm which depends on the ratio between the contour length and the persistence length. We find that both methods yield a

relaxation time of approximately 0.1-1  $\mu$ s for individual PII-2T polymers (depending on the number-average or weightaverage molecular weight). This would require an extensional strain rate >10<sup>6</sup> s<sup>-1</sup> to align the individual polymer chains, which is greater than the extensional strain rates explored in this work. Although we have characterized the radius of the PII-2T fibril aggregates in CB through SAXS (~10 nm), their lengths are not determinable from SAXS. Treating the fibrils as rodlike aggregates with lengths ranging from 100 nm to 1  $\mu$ m, as seen from freeze-dried SEM imaging, the orientational relaxation time then falls within the broad range of  $\sim 10 \ \mu s$  to 10 ms. However, considering that the estimated relaxation time for individual polymers is  $\sim 0.1$  to 1  $\mu s$  and that the experimental peak relaxation times range from 60 to >100  $\mu$ s from 3 to 10 mg/mL, it is likely that the flow-induced alignment and observed retardance stem primarily from alignment of the fibril aggregates in the CB solution as opposed to individual polymer chains.

#### CONCLUSIONS

By accessing high shear and extensional strain rates with our microfluidic devices and measuring the flow-induced retardance of our conjugated polymer systems, we were able to quantitatively characterize the dependence of flow-induced alignment on the flow type as well as the solution state properties. We have shown that there are several key factors to consider regarding flow-induced alignment arising from the combined effect of flow, solution aggregation, and concentration. First, we have shown that extensional flow is significantly more effective at aligning our conjugated polymer aggregates compared to shear flow. While the concept of shearing is commonly used in solution processing, so much so that blade coating is often termed "solution shearing", the incorporation of extensional flow in the deposition process is a promising method toward leveraging fluid flow to efficiently align conjugated polymers and aggregates. Second, we have shown that solution aggregation is an important factor for achieving flow-induced alignment. Individual, shorter polymer chains require extremely strong flows to align but the presence of aggregates makes it more feasible. Furthermore, the precise nature of the aggregation is of great consequence as forming larger, more rigid aggregates can make alignment significantly

easier to achieve. However, the internal structure achieved by aggregation may potentially limit the degree of orientational order the material can achieve at high strain rates. Finally, we have shown that concentration regimes, or more specifically the emergence of interaggregate interactions, is an important consideration when designing flow. As interactions between polymers and/or fibril aggregates emerge with increasing concentration, the effectiveness of flow to induce alignment diminishes. In solution processing of conjugated polymers where solvent evaporation occurs, the concentration rises drastically as the initial (semi)dilute solution traverses a complex pathway toward a solid film. It is then important to consider exactly at what point during this process flow is used to maximize its effectiveness and potentially alter the multiscale assembly pathway. Because concentration increases during the printing process and the initial concentration dictates film thickness, tuning flow and aggregation present a more controllable means of influencing alignment and subsequent morphology. These factors should absolutely be considered since aggregation is inherent to conjugated polymers and flow is inherent to solution processing. Therefore, the types of flows and strain rates during solution processing should be well understood and designed if possible. Aggregation can then be tuned by solvent choice or preprocessing to achieve an aggregate structure that is easy to align yet has an internal structure that is already highly ordered or can be modified by flow to achieve high order. These findings give insight toward designing both the aggregation structure of conjugated polymers and the fluid flows inherent to solution processing to produce a synergy that can enhance alignment and the subsequent electronic performance of conjugated polymer thin films.

#### ASSOCIATED CONTENT

#### **Solution** Supporting Information

The Supporting Information is available free of charge at https://pubs.acs.org/doi/10.1021/acs.macromol.2c01359.

Microfluidic device fabrication; retardance measurement theory; PII-2T aggregation and agglomeration in CB/DMF; un-normalized retardance vs concentration (PDF)

#### AUTHOR INFORMATION

#### **Corresponding Author**

Ying Diao — Department of Materials Science and Engineering, University of Illinois at Urbana—Champaign, Urbana, Illinois 61801, United States; Department of Chemical and Biomolecular Engineering, University of Illinois at Urbana—Champaign, Urbana, Illinois 61801, United States; Beckman Institute, Molecular Science and Engineering, University of Illinois at Urbana—Champaign, Urbana, Illinois 61801, United States; Frederick Seitz Materials Research Laboratory, University of Illinois at Urbana—Champaign, Urbana, Illinois 61801, United States; orcid.org/0000-0002-8984-0051; Email: yingdiao@illinois.edu

#### **Authors**

Justin J. Kwok – Department of Materials Science and Engineering, University of Illinois at Urbana–Champaign, Urbana, Illinois 61801, United States; ⊚ orcid.org/0000-0003-3909-4369

Giridar Vishwanathan — Department of Mechanical Science and Engineering, University of Illinois at

Urbana–Champaign, Urbana, Illinois 61801, United States Kyung Sun Park – Department of Chemical and Biomolecular

Engineering, University of Illinois at Urbana—Champaign, Urbana, Illinois 61801, United States

Bijal B. Patel – Department of Chemical and Biomolecular Engineering, University of Illinois at Urbana–Champaign, Urbana, Illinois 61801, United States

**Dongqi Zhao** – Department of Chemical and Biomolecular Engineering, University of Illinois at Urbana–Champaign, Urbana, Illinois 61801, United States

Gabriel Juarez – Department of Mechanical Science and Engineering, University of Illinois at Urbana–Champaign, Urbana, Illinois 61801, United States; orcid.org/0000-0002-5854-6925

Complete contact information is available at: https://pubs.acs.org/10.1021/acs.macromol.2c01359

#### Notes

The authors declare no competing financial interest.

#### ACKNOWLEDGMENTS

J.J.K. and Y.D. acknowledge support by the NSF CAREER award under grant #18-47828. J.J.K. also acknowledges support from the U.S. Department of Energy, Office of Science, Office of Workforce Development for Teachers and Scientists, Office of Science Graduate Student Research (SCGSR) program. The SCGSR program is administered by the Oak Ridge Institute for Science and Education for the DOE under contract number DE-SC0014664. K.S.P. and Y.D. acknowledge ONR support under Grant No. N00014-19-1-2146 and Grant No. N00014-22-1-2202, and K.S.P. acknowledges partial support from the Shen Postdoctoral Fellowship. B.B.P. and Y.D. acknowledge NSF DMREF for funding, under Grant Number 17-27605. This research used resources of the Advanced Photon Source, a U.S. Department of Energy (DOE) Office of Science User Facility, operated for the DOE Office of Science by Argonne National Laboratory under Contract No. DE-AC02-06CH11357. Extraordinary facility operations were supported in part by the DOE Office of Science through the National Virtual Biotechnology Laboratory, a consortium of DOE national laboratories focused on the response to COVID-19, with funding provided by the Coronavirus CARES Act.

#### REFERENCES

- (1) Wang, G.; Persson, N.; Chu, P.-H.; Kleinhenz, N.; Fu, B.; Chang, M.; Deb, N.; Mao, Y.; Wang, H.; Grover, M. A.; Reichmanis, E. Microfluidic Crystal Engineering of  $\pi$ -Conjugated Polymers. *ACS Nano* **2015**, *9* (8), 8220–8230.
- (2) Wang, G.; Chu, P.-H.; Fu, B.; He, Z.; Kleinhenz, N.; Yuan, Z.; Mao, Y.; Wang, H.; Reichmanis, E. Conjugated Polymer Alignment: Synergisms Derived from Microfluidic Shear Design and UV Irradiation. ACS Appl. Mater. Interfaces 2016, 8 (37), 24761–24772.
- (3) Chang, M.; Choi, D.; Egap, E. Macroscopic Alignment of One-Dimensional Conjugated Polymer Nanocrystallites for High-Mobility Organic Field-Effect Transistors. *ACS Appl. Mater. Interfaces* **2016**, 8 (21), 13484–13491.
- (4) Choi, D.; Chang, M.; Reichmanis, E. Controlled Assembly of Poly(3-Hexylthiophene): Managing the Disorder to Order Transition on the Nano- through Meso-Scales. *Adv. Funct. Mater.* **2015**, 25 (6), 920–927.
- (5) Xi, Y.; Li, D. S.; Newbloom, G. M.; Tatum, W. K.; O'Donnell, M.; Luscombe, C. K.; Pozzo, L. D. Sonocrystallization of Conjugated

- Polymers with Ultrasound Fields. Soft Matter 2018, 14 (24), 4963–4976.
- (6) Li, M.; An, C.; Marszalek, T.; Baumgarten, M.; Yan, H.; Müllen, K.; Pisula, W. Controlling the Surface Organization of Conjugated Donor-Acceptor Polymers by Their Aggregation in Solution. *Adv. Mater.* **2016**, 28 (42), 9430–9438.
- (7) Li, M.; Bin, H.; Jiao, X.; Wienk, M. M.; Yan, H.; Janssen, R. A. J. Controlling the Microstructure of Conjugated Polymers in High-Mobility Monolayer Transistors via the Dissolution Temperature. *Angew. Chem., Int. Ed.* **2020**, *59* (2), 846–852.
- (8) Luzio, A.; Criante, L.; D'Innocenzo, V.; Caironi, M. Control of Charge Transport in a Semiconducting Copolymer by Solvent-Induced Long-Range Order. Sci. Rep. 2013, 3 (1), 3425.
- (9) Trefz, D.; Gross, Y. M.; Dingler, C.; Tkachov, R.; Hamidi-Sakr, A.; Kiriy, A.; McNeill, C. R.; Brinkmann, M.; Ludwigs, S. Tuning Orientational Order of Highly Aggregating P(NDI2OD-T2) by Solvent Vapor Annealing and Blade Coating. *Macromolecules* **2019**, 52 (1), 43–54.
- (10) Xu, Z.; Park, K. S.; Diao, Y. What Is the Assembly Pathway of a Conjugated Polymer From Solution to Thin Films? *Frontiers in Chemistry* **2020**, *8*, 1194.
- (11) Park, K. S.; Kwok, J. J.; Kafle, P.; Diao, Y. When Assembly Meets Processing: Tuning Multiscale Morphology of Printed Conjugated Polymers for Controlled Charge Transport. *Chem. Mater.* **2021**, 33 (2), 469–498.
- (12) Shaw, L.; Hayoz, P.; Diao, Y.; Reinspach, J. A.; To, J. W. F.; Toney, M. F.; Weitz, R. T.; Bao, Z. Direct Uniaxial Alignment of a Donor-Acceptor Semiconducting Polymer Using Single-Step Solution Shearing. ACS Appl. Mater. Interfaces 2016, 8, 9285.
- (13) Shaw, L.; Yan, H.; Gu, X.; Hayoz, P.; Weitz, R. T.; Kaelblein, D.; Toney, M. F.; Bao, Z. Microstructural Evolution of the Thin Films of a Donor-Acceptor Semiconducting Polymer Deposited by Meniscus-Guided Coating. *Macromolecules* **2018**, *51* (11), 4325–4340
- (14) Diao, Y.; Zhou, Y.; Kurosawa, T.; Shaw, L.; Wang, C.; Park, S.; Guo, Y.; Reinspach, J. A.; Gu, K.; Gu, X.; Tee, B. C. K.; Pang, C.; Yan, H.; Zhao, D.; Toney, M. F.; Mannsfeld, S. C. B.; Bao, Z. Flow-Enhanced Solution Printing of All-Polymer Solar Cells. *Nat. Commun.* **2015**, *6*, 7955.
- (15) Xu, J.; Wu, H.-C.; Zhu, C.; Ehrlich, A.; Shaw, L.; Nikolka, M.; Wang, S.; Molina-Lopez, F.; Gu, X.; Luo, S.; Zhou, D.; Kim, Y.-H.; Wang, G.-J. N.; Gu, K.; Feig, V. R.; Chen, S.; Kim, Y.; Katsumata, T.; Zheng, Y.-Q.; Yan, H.; Chung, J. W.; Lopez, J.; Murmann, B.; Bao, Z. Multi-Scale Ordering in Highly Stretchable Polymer Semiconducting Films. *Nat. Mater.* **2019**, *18* (6), 594–601.
- (16) Wang, G.; Feng, L.-W.; Huang, W.; Mukherjee, S.; Chen, Y.; Shen, D.; Wang, B.; Strzalka, J.; Zheng, D.; Melkonyan, F. S.; Yan, J.; Stoddart, J. F.; Fabiano, S.; DeLongchamp, D. M.; Zhu, M.; Facchetti, A.; Marks, T. J. Mixed-Flow Design for Microfluidic Printing of Two-Component Polymer Semiconductor Systems. *Proc. Natl. Acad. Sci. U. S. A.* 2020, 117 (30), 17551–17557.
- (17) Qu, G.; Kwok, J. J.; Diao, Y. Flow-Directed Crystallization for Printed Electronics. *Acc. Chem. Res.* **2016**, 49 (12), 2756–2764.
- (18) Patel, B. B.; Diao, Y. Multiscale Assembly of Solution-Processed Organic Electronics: The Critical Roles of Confinement, Fluid Flow, and Interfaces. *Nanotechnology* **2018**, 29 (4), 044004.
- (19) Wie, J. J.; Nguyen, N. A.; Cwalina, C. D.; Liu, J.; Martin, D. C.; Mackay, M. E. Shear-Induced Solution Crystallization of Poly(3-Hexylthiophene) (P3HT). *Macromolecules* **2014**, *47* (10), 3343–3349.
- (20) Park, K. S.; Kwok, J. J.; Dilmurat, R.; Qu, G.; Kafle, P.; Luo, X.; Jung, S.-H.; Olivier, Y.; Lee, J.-K.; Mei, J.; Beljonne, D.; Diao, Y. Tuning Conformation, Assembly, and Charge Transport Properties of Conjugated Polymers by Printing Flow. *Science Advances* **2019**, *5* (8), No. eaaw7757.
- (21) Fuller, G. G.; Leal, L. G. Flow Birefringence of Dilute Polymer Solutions in Two-Dimensional Flows. *Rheol. Acta* **1980**, *19* (5), 580–600.

- (22) Fuller, G. G.; Leal, L. G. Flow Birefringence of Concentrated Polymer Solutions in Two-Dimensional Flows. *J. Polym. Sci., Polym. Phys. Ed.* 1981, 19 (4), 557–587.
- (23) Keller, A.; Kolnaar, H. W. H.Flow-Induced Orientation and Structure Formation. In *Materials Science and Technology*; Wiley-VCH Verlag GmbH & Co. KGaA: 2006.
- (24) Odell, J. A.; Keller, A.; Müller, A. J.Extensional Flow Behavior of Macromolecules in Solution. In *Polymers in Aqueous Media*; Glass, J. E., Ed.; American Chemical Society: Washington, DC, 1989; Vol. 223, pp 193–244.
- (25) Pathak, J. A.; Hudson, S. D. Rheo-Optics of Equilibrium Polymer Solutions: Wormlike Micelles in Elongational Flow in a Microfluidic Cross-Slot. *Macromolecules* **2006**, 39 (25), 8782–8792.
- (26) Ober, T. J.; Soulages, J.; McKinley, G. H. Spatially Resolved Quantitative Rheo-Optics of Complex Fluids in a Microfluidic Device. *J. Rheol.* **2011**, 55 (5), 1127–1159.
- (27) Sun, C.; Huang, H.-Y. Measurements of Flow-Induced Birefringence in Microfluidics. *Biomicrofluidics* **2016**, *10* (1), 011903.
- (28) Haward, S. J.; Oliveira, M. S. N.; Alves, M. A.; McKinley, G. H. Optimized Cross-Slot Flow Geometry for Microfluidic Extensional Rheometry. *Phys. Rev. Lett.* **2012**, *109* (12), 128301.
- (29) Haward, S. J. Characterization of Hyaluronic Acid and Synovial Fluid in Stagnation Point Elongational Flow. *Biopolymers* **2014**, *101* (3), 287–305.
- (30) Haward, S. J. Synovial Fluid Response to Extensional Flow: Effects of Dilution and Intermolecular Interactions. *PLoS One* **2014**, 9 (3), No. e92867.
- (31) Haward, S. J. Microfluidic Extensional Rheometry Using Stagnation Point Flow. *Biomicrofluidics* **2016**, *10* (4), 043401.
- (32) Haward, S. J.; Odell, J. A.; Li, Z.; Yuan, X.-F. The Rheology of Polymer Solution Elastic Strands in Extensional Flow. *Rheol. Acta* **2010**, 49 (7), 781–788.
- (33) Haward, S. J.; Sharma, V.; Odell, J. A. Extensional Opto-Rheometry with Biofluids and Ultra-Dilute Polymer Solutions. *Soft Matter* **2011**, 7 (21), 9908.
- (34) Haward, S. J.; Ober, T. J.; Oliveira, M. S. N.; Alves, M. A.; McKinley, G. H. Extensional Rheology and Elastic Instabilities of a Wormlike Micellar Solution in a Microfluidic Cross-Slot Device. *Soft Matter* **2012**, *8* (2), 536–555.
- (35) Haward, S. J.; Jaishankar, A.; Oliveira, M. S. N.; Alves, M. A.; McKinley, G. H. Extensional Flow of Hyaluronic Acid Solutions in an Optimized Microfluidic Cross-Slot Device. *Biomicrofluidics* **2013**, 7 (4), 044108.
- (36) Haward, S. J.; McKinley, G. H.; Shen, A. Q. Elastic Instabilities in Planar Elongational Flow of Monodisperse Polymer Solutions. *Sci. Rep.* **2016**, *6*, srep.3029.
- (37) Del Giudice, F.; Haward, S. J.; Shen, A. Q. Relaxation Time of Dilute Polymer Solutions: A Microfluidic Approach. *J. Rheol.* **2017**, *61* (2), 327–337.
- (38) Calabrese, V.; Haward, S. J.; Shen, A. Q. Effects of Shearing and Extensional Flows on the Alignment of Colloidal Rods. *Macromolecules* **2021**, 54 (9), 4176–4185.
- (39) Li, Q.-Y.; Yao, Z.-F.; Lu, Y.; Zhang, S.; Ahmad, Z.; Wang, J.-Y.; Gu, X.; Pei, J. Achieving High Alignment of Conjugated Polymers by Controlled Dip-Coating. *Adv. Electron. Mater.* **2020**, *6* (6), 2000080. (40) Zhou, Y.; Kurosawa, T.; Ma, W.; Guo, Y.; Fang, L.; Vandewal, K.; Diao, Y.; Wang, C.; Yan, Q.; Reinspach, J.; Mei, J.; Appleton, A. L.; Koleilat, G. I.; Gao, Y.; Mannsfeld, S. C. B.; Salleo, A.; Ade, H.; Zhao, D.; Bao, Z. High Performance All-Polymer Solar Cell via Polymer Side-Chain Engineering. *Adv. Mater.* **2014**, *26* (22), 3767–3772.
- (41) Kim, D. H.; Ayzner, A. L.; Appleton, A. L.; Schmidt, K.; Mei, J.; Toney, M. F.; Bao, Z. Comparison of the Photovoltaic Characteristics and Nanostructure of Fullerenes Blended with Conjugated Polymers with Siloxane-Terminated and Branched Aliphatic Side Chains. *Chem. Mater.* **2013**, 25 (3), 431–440.
- (42) Wei, X.; Zhang, W.; Yu, G. Semiconducting Polymers Based on Isoindigo and Its Derivatives: Synthetic Tactics, Structural Mod-

ifications, and Applications. Adv. Funct. Mater. 2021, 31 (21), 2010979.

- (43) Kwok, J. J.; Park, K. S.; Patel, B. B.; Dilmurat, R.; Beljonne, D.; Zuo, X.; Lee, B.; Diao, Y. Understanding Solution State Conformation and Aggregate Structure of Conjugated Polymers via Small Angle X-Ray Scattering. *Macromolecules* **2022**, *55* (11), 4353–4366.
- (44) Lei, T.; Dou, J.-H.; Pei, J. Influence of Alkyl Chain Branching Positions on the Hole Mobilities of Polymer Thin-Film Transistors. *Adv. Mater.* **2012**, 24 (48), 6457–6461.
- (45) Keller, A.; Miiller, A. J.; Odell, J. A. Entanglements in Semi-Dilute Solutions as Revealed by Elongational Flow Studies. *Prog. Colloid Polym. Sci.* 1987, 75, 179–200.
- (46) Harlen, O. G.; Hinch, E. J.; Rallison, J. M. Birefringent Pipes: The Steady Flow of a Dilute Polymer Solution near a Stagnation Point. *J. Non-Newtonian Fluid Mech.* **1992**, 44, 229–265.
- (47) Tivol, W. F.; Briegel, A.; Jensen, G. J. An Improved Cryogen for Plunge Freezing. *Microsc Microanal* **2008**, *14* (5), 375–379.
- (48) Srivastava, N.; Burns, M. A. Analysis of Non-Newtonian Liquids Using a Microfluidic Capillary Viscometer. *Anal. Chem.* **2006**, 78 (5), 1690–1696.
- (49) Bahrami, M.; Yovanovich, M. M.; Culham, J. R. Pressure Drop of Fully-Developed, Laminar Flow in Microchannels of Arbitrary Cross-Section. *Journal of Fluids Engineering* **2006**, *128* (5), 1036.
- (50) Dhont Jan, K. G.; Briels Wim, J. Rod-Like Brownian Particles in Shear Flow: Sections 3.1 3.9. *Soft Matter* **2007**, DOI: 10.1002/9783527617067.ch3a.
- (51) Nahid, M. M.; Welford, A.; Gann, E.; Thomsen, L.; Sharma, K. P.; McNeill, C. R. Nature and Extent of Solution Aggregation Determines the Performance of P(NDI2OD-T2) Thin-Film Transistors. *Adv. Electron. Mater.* **2018**, DOI: 10.1002/aelm.201700559.
- (52) Xi, Y.; Wolf, C. M.; Pozzo, L. D. Self-Assembly of Donor-Acceptor Conjugated Polymers Induced by Miscible 'Poor' Solvents. *Soft Matter* **2019**, *15* (8), 1799–1812.
- (53) Prosa, T. J.; Moulton, J.; Heeger, A. J.; Winokur, M. J. Diffraction Line-Shape Analysis of Poly(3-Dodecylthiophene): A Study of Layer Disorder through the Liquid Crystalline Polymer Transition. *Macromolecules* **1999**, 32 (12), 4000–4009.
- (54) Rivnay, J.; Noriega, R.; Kline, R. J.; Salleo, A.; Toney, M. F. Quantitative Analysis of Lattice Disorder and Crystallite Size in Organic Semiconductor Thin Films. *Phys. Rev. B* **2011**, 84 (4), 045203
- (55) Broersma, S. Rotational Diffusion Constant of a Cylindrical Particle. *J. Chem. Phys.* **1960**, 32 (6), 1626–1631.
- (56) Hagerman, P. J.; Zimm, B. H. Monte Carlo Approach to the Analysis of the Rotational Diffusion of Wormlike Chains. *Biopolymers* **1981**, 20 (7), 1481–1502.
- (57) Miura, T.; Kishi, R.; Mikami, M.; Tanabe, Y. Effect of Rigidity on the Crystallization Processes of Short Polymer Melts. *Phys. Rev. E* **2001**, *63* (6), 061807.
- (58) Ng, R. C. -Y.; Leal, L. G. Concentration Effects on Birefringence and Flow Modification of Semidilute Polymer Solutions in Extensional Flows. *J. Rheol.* **1993**, *37* (3), 443–468.
- (59) Springer Handbook of Experimental Fluid Mechanics; Tropea, C., Yarin, A. L., Foss, J. F., Eds.; Springer: Berlin, 2007.
- (60) Hsiao, K.-W.; Sasmal, C.; Ravi Prakash, J.; Schroeder, C. M. Direct Observation of DNA Dynamics in Semidilute Solutions in Extensional Flow. *J. Rheol.* **2017**, *61* (1), 151–167.
- (61) Perkins, T. T.; Smith, D. E.; Chu, S. Single Polymer Dynamics in an Elongational Flow. *Science* **1997**, 276 (5321), 2016–2021.
- (62) Schroeder, C. M.; Babcock, H. P.; Shaqfeh, E. S. G.; Chu, S. Observation of Polymer Conformation Hysteresis in Extensional Flow. *Science* **2003**, *301* (5639), 1515–1519.
- (63) Doi, M. Molecular Dynamics and Rheological Properties of Concentrated Solutions of Rodlike Polymers in Isotropic and Liquid Crystalline Phases. *J. Polym. Sci., Polym. Phys. Ed.* **1981**, 19 (2), 229–243.
- (64) Håkansson, K. M. O.; Lundell, F.; Prahl-Wittberg, L.; Söderberg, L. D. Nanofibril Alignment in Flow Focusing: Measurements and Calculations. *J. Phys. Chem. B* **2016**, 120 (27), 6674–6686.

(65) Clasen, C.; Plog, J. P.; Kulicke, W.-M.; Owens, M.; Macosko, C.; Scriven, L. E.; Verani, M.; McKinley, G. H. How Dilute Are Dilute Solutions in Extensional Flows? *J. Rheol.* **2006**, *50* (6), 849.

### **□** Recommended by ACS

#### Pursuing Phase Transitions of a Concentrated Polymer Solution by In Situ Fluorescence Measurements Based On Aggregation-Induced Emission

Zhen-zhen Fu, Qiang Fu, et al.

OCTOBER 17, 2022

THE JOURNAL OF PHYSICAL CHEMISTRY LETTERS

READ 🗹

# Structure of Self-Initiated Photopolymerized Films: A Comparison of Models

Béla Nagy, Thomas Ederth, et al.

NOVEMBER 03, 2022

LANGMUIR

READ 🗹

## Polymer Molecular Weight Determination via Fluorescence Lifetime

Antonio Garcia IV and Suzanne A. Blum

DECEMBER 02, 2022

JOURNAL OF THE AMERICAN CHEMICAL SOCIETY

RFAD [✓

# Fluorescence Technique Lighting the Particle Migration in Polymers

Qi Xu, Chao Lu, et al.

JUNE 17, 2022

MACROMOLECULES

READ 🗹

Get More Suggestions >